Alumina Failure and Post-failure Oxidation in the NiCoCrAlY Alloy System at High Temperature

Thomas Gheno, Catherine Rio, Maxime Ecochard, Damien Texier

Alumina failure and post-failure oxidation in the NiCoCrAlY alloy system at high temperature

Thomas Gheno[1], Catherine Rio[1], Maxime Ecochard[2] and Damien Texier[2]

[1] *DMAS, ONERA, Université Paris Saclay, 92322 Chatillon, France*

[2] *Institut Clement Ader (ICA) - UMR CNRS 5312, Université de Toulouse, CNRS, INSA, UPS, Mines Albi, ISAE-SUPAERO, Campus Jarlard, 81013 Albi Cedex 09, France*

email: thomas.gheno at onera.fr

This is a post-peer-review, pre-copyedit version of an article published in Oxidation of Metals. The final version is available online at:
https://doi.org/10.1007/s11085-021-10060-9

Abstract This paper examines the oxidation behavior of thin specimens of cast NiCoCrAlY alloys at 1150 °C through successive stages, from Al_2O_3 growth to complete alloy conversion to oxide. Five alloy compositions were used, with varying fractions and compositions of γ and β. The time evolution of the alloy composition during Al_2O_3 growth was simulated using the DICTRA module of Thermo-Calc, and calculated analytically in the approximation of flat profiles. Simulated and experimental profiles were found to be in good agreement, indicating that the phase equilibrium and mass balance were correctly reproduced in the simulations. Local variations of alloy composition were observed in thinner specimens and found to be comparable with the variations expected from the uncertainty on the initial specimen thickness. The variations observed in the time-to-Al_2O_3 failure were greater than expected on this basis, suggesting that additional sources of variability were in effect. Alumina failure was followed by the growth of a Cr_2O_3 layer at the alloy–scale interface. Similarly, Cr consumption eventually led to Cr_2O_3 failure, and Ni- and Co-containing spinel oxide formed, converting the Cr_2O_3 at the alloy–scale interface and the Al_2O_3 at the scale–gas interface. The remaining NiCo alloy was then converted to (Ni,Co)O. This sequence occurred without abrupt increase of the mass gain, due to the continued presence of the remnant Al_2O_3 layer, and to the small amount of metal left to oxidize when the (Ni,Co)O eventually broke through the scale. The evolution of the scale composition throughout the oxidation stages is discussed based on an analysis of the thermodynamic conditions at the alloy–scale interface.

Keywords Selective oxidation; Reservoir effect; Thin foils; Intrinsic chemical failure; Breakaway; Alloy diffusion

1 Introduction

High temperature alloys and coatings withstand oxidizing environments via selective oxidation, a process in which an alloying element, usually Cr or Al, is preferentially oxidized to form a slow-growing and adherent oxide scale — oxidation is then protective. The corrosion rates associated with the oxidation of major elements such as Fe, Ni or Co, and with attacks from other oxidants such as C or S, are orders of magnitude larger than those imparted by protective oxidation. As a consequence, what are the conditions of protective oxidation is a question of technological importance, one that has attracted considerable attention [1].

The present paper is interested in protection by Al_2O_3 but the following would apply similarly to Cr_2O_3. Alumina develops as an external scale rather than internal precipitates when the outward Al flux in the alloy exceeds the inward O flux [2, 3]. Once the Al_2O_3 scale is formed, the Al concentration at the alloy-scale interface, x_{Al}^{int}, must remain above a certain threshold, noted x_{Al}^{*}, for Al_2O_3 to be thermodynamically stable. This threshold is determined by the equilibrium between Al_2O_3 and the next most stable oxide, usually Cr_2O_3 if the alloy also contains Cr. At steady-state, the scale stability is achieved when the outward Al flux matches the Al flux required for scale growth [4]. In the ideal case of a strictly parabolic scale growth on a binary alloy of composition-independent diffusion properties, once a steady-state is reached, the interfacial Al concentration remains constant [4]. In the absence of external causes for change, this remains so until Al depletion reaches the center of the specimen, at which point x_{Al}^{int} gradually decreases. In practice, non-parabolic oxidation kinetics as well as composition-dependent alloy diffusion properties may cause x_{Al}^{int} to increase or decrease during steady-state.

The classification introduced by Evans et al. [5] distinguishes intrinsic and extrinsic forms of chemical failure. When the protective scale is subject to mechanical damage (cracks or delamination), its re-formation rapidly consumes the oxide-forming element (say, Al), and x_{Al}^{int} drops. Mechanically-induced chemical failure (MICF) occurs if x_{Al}^{int} falls below x_{Al}^{*}, after either one or repeated such events. MICF is essentially a local form of failure — although it could in principle be global if the scale were to spall off everywhere at the same time. On the other hand, intrinsic chemical failure (InCF) occurs when $x_{Al}^{int} < x_{Al}^{*}$ everywhere on the surface, either shortly after the start of oxidation (no protective regime is reached), or, if the specimen is thin enough, after Al depletion has reached the center of the specimen, and x_{Al}^{int} has eventually reached x_{Al}^{*} ("time-delayed InCF"). Before causing InCF, the global decrease of x_{Al}^{int} due to through-thickness depletion also has the effect of increasing the likelihood of local failure by MICF.

When designing thin components such as turbine blades, heat exchangers, heaters or catalyst carriers, the question of through-thickness depletion can arise, and it is desirable to be able to predict the time-to-failure, given a set of service conditions. This becomes even more relevant as additive manufacturing fosters the fabrication of components with more intricate geometries and therefore thinner sections. This question is also central in the design of alloy-coating systems. An Al-rich coating will tend to lose Al by oxidation on one side and by interdiffusion with the alloy on the other. As in the case of a bare alloy oxidizing on both sides, a change of boundary conditions occurs when the two Al depletion profiles meet, and x_{Al}^{int} tends to decrease. Eventually, the Al loss by oxidation can be so important that the alloy-coating flux is reversed, and the coating receives Al from the alloy. It is important to anticipate these evolutions because they directly control the oxidation lifetime, but also because changes in the alloy composition via alloy-coating interdiffusion may affect the mechanical properties of the system [6].

Different types of models have been developed to estimate the time-to-failure of a protective scale, depending on the shape of the depletion profile. If Al diffusion in the alloy is much faster than the oxidation rate, the Al profile is essentially flat, and failure occurs when Al has been fully consumed. The time-to-failure is then obtained from a relatively simple mass balance, as shown by Quadakkers and Bongartz [7]. The situation is more complex if the Al profile is not flat, and there is

significant Al left in the bulk when $x_{\mathrm{Al}}^{\mathrm{int}}$ reaches x_{Al}^{*}. Estimating the time-to-failure then requires a model describing the time evolution of the Al profile, a problem that has been studied under various limiting assumptions, using analytical and numerical methods — the reader is referred to Refs. [8, 9, 10] for reviews of earlier and more recent literature on the subject. Various approaches can then be used to define and estimate a time-to-failure, as shown recently by Duan et al. [11] for instance.

When Al_2O_3 can no longer be formed, oxides of the other alloying elements form instead. This transition (or the post-transition stage) is commonly called breakaway, in reference to the sudden increase of the oxidation rate, usually manifested in a sudden increase of the mass gain. In some circumstances, however, Al_2O_3 remains as a continuous layer in the scale and continues to limit the overall oxidation rate for a significant amount of time, giving rise to a secondary protective stage. Slow growth of a Cr_2O_3 layer at the base of the scale, termed "pseudo-protection" in Ref. [12], has been reported on thin foils of FeCrAl alloys [13, 14, 15, 16, 17, 18] and of a wrought γ-phase NiCrAl alloy [19, 20].

Alumina failure on MCrAlY coatings has been observed [21, 22] but so far, detailed examinations of alloy and scale composition in pre- and post-failure stages have mostly concerned single-phase alloys. Recently, InCF has been studied in thin freestanding specimens of a multiphase APS NiCoCrAlY coating [23]. The reaction kinetics in Ref. [23] were affected by metallurgical defects inherent to the projection process. The aim of the present paper is to provide a more quantitative analysis of alloy composition variations and phase transformations in response to oxidation, and a more systematic description of the time-to-failure and post-failure reaction mechanisms in the NiCoCrAlY alloy system. This was done based on γ, γ–β and β NiCoCrAlY alloys with varying phase fractions and compositions. Oxidation experiments were carried out using thin specimens at 1150 °C so as to trigger Al_2O_3 failure in relatively short times. The mode of failure that applied in these conditions was InCF. The experimental work was completed with numerical simulations of the alloy composition using the DICTRA module of Thermo-Calc [24].

2 Materials and procedures

2.1 Materials

Five cast NiCoCrAlY alloys were used in this study. The nominal compositions are given in Table 1 and plotted on an isothermal, isoplethal section of the NiCoCrAl phase diagram in Fig. 1. At 1150 °C, alloys UT2, UT4 and UT11 have a two-phase γ–β microstructure, while UT13 and UT17 are single-phase (γ and β, respectively). Alloys UT13, UT11 and UT17 are approximately located on the same tie-line, i.e., the composition of the γ and β phases in UT11 are the compositions of UT13 and UT17, respectively. Conversely, alloys UT2 and UT11 have similar phase fractions, but different phase compositions (for more details on how the alloys were designed, the reader is referred to Ref. [25]). Alloys with varying Al and Cr contents were used to cover a wide composition range.

Ingots were made by argon-arc melting, followed by drop casting into 10 mm diameter rods, which were then homogenized in vacuum for 6 h at 1200 °C plus another 48 h at 1150 °C, at the Materials Preparation Center of the Ames Laboratory [28]. Microstructural characterization after further annealing at 1150 °C

Table 1: Nominal composition of the MCrAlY alloys (at. %).

Ref.	Ni	Co	Cr	Al	Y	Phases at 1150 °C
UT2	bal.	19	15	24	0.1	γ–β
UT4	bal.	30	30	12	0.1	γ–β
UT11	bal.	19	10	24	0.1	γ–β
UT13	bal.	28	19	11	0.1	γ
UT17	bal.	14	5	32	0.1	β

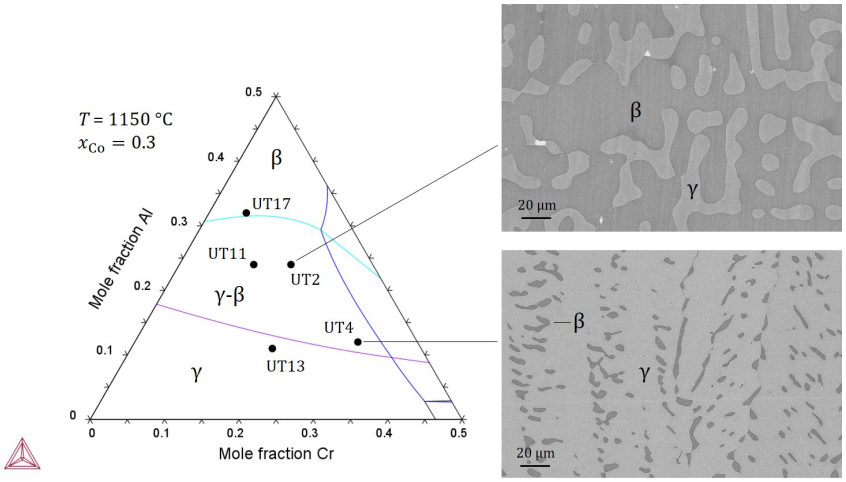

Figure 1: Nominal alloy compositions projected on an isothermal, isoplethal section (T =1150 °C, $x_{\mathrm{Co}} = 0.3$) of the NiCoCrAl phase diagram, calculated with Thermo-Calc [24] and the CRALDAD database [26, 27]. Note that not all alloys are on the $x_{\mathrm{Co}} = 0.3$ isopleth. SEM micrographs showing the bulk microstructure of 2-phase alloys are also included.

followed by air cooling showed that the phases present were those expected from thermodynamic equilibrium. Two SEM micrographs are included in Fig. 1 as examples. The alloys also contained a small amount of yttrium-rich intermetallics ($\sim$ 0.1 vol. %).

2.2 Experimental procedures

The rods were sliced using electrodischarge machining to obtain 1-mm thick discs. Thin specimens were then prepared using a precision jig and a lapping machine in order to ensure good control over the thickness and surface finish [29]. Four specimens were prepared for each alloy: one "thick" (400–500 µm) used as a reference (series A in Table 2), and three "thin" ($<$ 50 µm) used to rapidly trigger InCF (series B, C and D). Within a specimen, the thickness variation was about $\pm$ 3 µm around the average.

The specimens were oxidized in laboratory air at 1150°C for 200 h, with interruptions after 20, 50 and 100 h. The specimens were weighed and photographed at each interruption.

After 200 h, the specimen surfaces were analyzed by X-ray diffraction (XRD)

Table 2: Average initial specimen thicknesses (µm). Variations within specimens were about ± 3 µm around the average.

Alloy	A	B	C	D
UT2	476	47	26	11
UT4	482	48	35	22
UT11	478	43	23	24
UT13	438	29	16	17
UT17	445	35		14

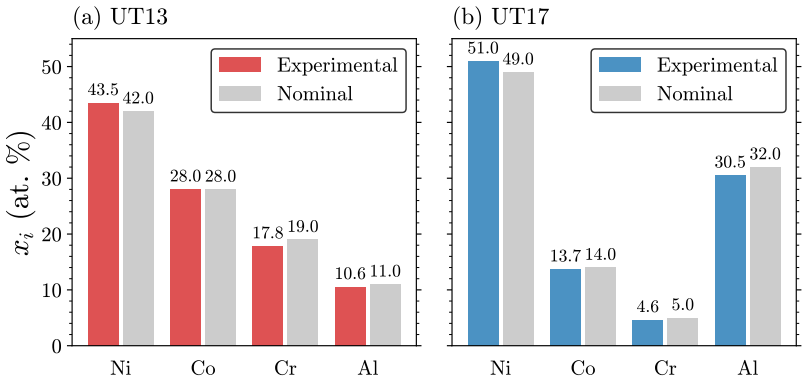

Figure 2: Compositions of single-phase alloys (a) UT13 (γ) and (b) UT17 (β) in the as-received state measured by SEM–EDS, compared with nominal compositions. (The experimental values represent the mean of 11 point analyses. The standard deviation for each series was about 0.1–0.2 at. %.)

using an X'Pert Panalytical diffractometer with a Cu-Kα radiation and a step size of 0.033 °. Metallographic cross-sections were then prepared and analyzed by scanning electron microscopy (SEM) in a FEG-SEM Zeiss Merlin. Chemical compositions were measured by energy dispersive X-ray spectrometry (EDS) using a built-in standardless quantification procedure (SAMx acquisition software). The compositions of single-phase alloys UT13 (γ) and UT17 (β) measured by EDS in the as-received state are compared with their nominal compositions in Fig. 2. The mean difference between EDS and nominal concentrations is 0.9 at. %. From previous work with alloys obtained from the same supplier, the actual compositions are known to be within 0.5 at. % of the nominal compositions. It is concluded that the accuracy of the EDS measurements is about 1 at. %. The oxide phases were identified based on the XRD and SEM–EDS results.

2.3 Simulation procedures

The oxidation-induced evolution of alloy composition was simulated by solving the multicomponent diffusion problem in the alloy, in one dimension, using the DICTRA module of Thermo-Calc [24]. The procedure is described in detail in Ref. [10]; aspects specific to the present simulations are addressed here.

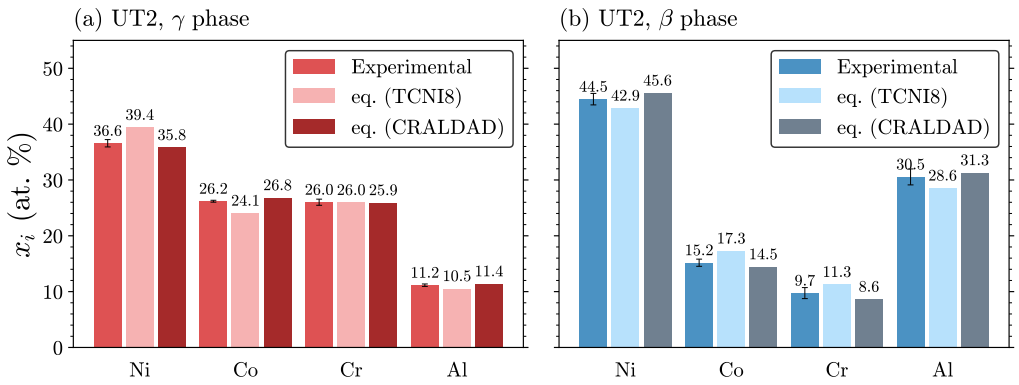

Figure 3: Phase compositions in γ–β alloy UT2 in the as-received state (annealed at 1150 °C) measured by SEM–EDS, compared with equilibrium values at 1150 °C calculated with Thermo-Calc and the TCNI8 and CRALDAD databases. (The experimental values represent the mean of 30 point analyses. The error bars represent the standard deviation for each series.)

Phase equilibria in bulk alloys and choice of databases

The DICTRA simulations combine phase equilibrium calculations and a finite-difference resolution of the diffusion equation. This requires thermodynamics and mobility databases, which store parameters used in computing the quantities of interest (Gibbs free energy and diffusion mobility) according to the CALPHAD method [30, 31].

The computations were run with MOBNI (version 5 [32]), the Ni-based alloy mobility database from Thermo-Calc Software. MOBNI is recommended for use with TCNI, the associated thermodynamics database. However, equilibrium phase compositions computed with TCNI (version 8 [33]) were found to be at variance with compositions measured in the γ–β alloys. This is due to the fact that TCNI is geared towards superalloy compositions, and is not adapted to the large Co, Cr and Al contents of the present alloys. A better representation of the γ–β equilibrium was obtained using CRALDAD, an open NiCoCrAl database developed specifically for bondcoat-type compositions [26, 27]. As an illustration, phase compositions measured by EDS in the UT2 alloy are compared with those calculated using both databases in Fig. 3. On average, the difference between calculated and experimental values is 1.6 at. % for TCNI8, versus 0.7 at. % for CRALDAD. For a detailed study of phase equilibria and database comparison in the NiCoCrAl system, the reader is referred to Ref. [26].

We note that since MOBNI was developed using thermodynamics data from TCNI, its use in association with another database results in diffusion properties that are not optimized. This should, in principle, be avoided. In the present case, however, alloy diffusion was fast relative to oxidation; this resulted in flat composition profiles that were not very sensitive to the diffusion properties. Indeed, tests conducted on the alloys of interest with the TCNI8 + MOBNI5 and CRALDAD + MOBNI5 combinations showed that the latter produced results in better agreement with the experimental data in two-phase alloys (because of the better description of

phase equilibrium), while there was no significant difference in single-phase alloys (because of the low sensitivity to the diffusivity). The results included in this paper were obtained with CRALDAD + MOBNI5.

To be complete, we also note that diffusion mobilities generated with MOBNI5 are in significant error in NiCoCrAl alloys with large Co concentrations [10] such as those considered here. However, for the reason stated above, this had no significant impact on the present simulations.

Oxidation model

The simulated material represented half-specimens, with a zero-flux boundary condition on the bulk side (symmetry plane). Oxidation was modeled by setting a flux of the oxidized element as a boundary condition on the surface side. The other element fluxes were set to zero. As a consequence, the total amount of matter in the simulation (and therefore the size of the simulated material) decreased over time, reflecting the metal recession associated with oxidation. The space grid was adjusted as required via a built-in procedure.

As shown subsequently, the alloys were subject to a sequence of stages, starting with Al_2O_3 growth, and ending with full metal conversion to oxide. The growth of a pure Al_2O_3 scale was considered first. The scales observed in practice contained small amounts of impurities, but this was neglected in the simulations for simplicity. Alumina growth was modeled using a simple power rate law,

$$X_{Al_2O_3}^n = k \cdot t, \tag{1}$$

where $X_{Al_2O_3}$ is the Al_2O_3 thickness, k the rate constant and t the time. Based on a mass balance at the alloy-scale interface, the Al flux across this interface, J_{Al}^{out}, can be expressed as

$$J_{Al}^{out} = \frac{2}{V_{Al_2O_3}} \frac{dX_{Al_2O_3}}{dt}, \tag{2}$$

with $V_{Al_2O_3}$ the molar volume of Al_2O_3. Using Eq. (1), this yields

$$J_{Al}^{out} = \frac{2}{V_{Al_2O_3}} \frac{k}{n} (k \cdot t)^{\frac{1}{n}-1}. \tag{3}$$

The boundary condition used in the simulation was given in terms of $J_{Al}^{out} \cdot V_a$, where V_a is the molar volume of the alloy.

The oxidation parameters were estimated to be $n = 3$ and $k = 3 \times 10^{-22}$ m^3/s, based on the mass gains measured on the specimens that exclusively formed Al_2O_3 throughout the 200 h experiment (Section 3.1). It is recognized that oxidation kinetics are in general more complex than Eq. (1), for a number of reasons. The transient stage includes rapid variations of the oxidation rate, which is arguably not well captured by a power law with constant parameters. The microstructural evolution of the Al_2O_3 will also introduce deviations from Eq. (1) — specifically, as grain boundary diffusion significantly contributes to mass transport in the scale, oxide grain growth will tend to accelerate the decrease of the oxidation rate and result in non-trivial thickening kinetics [34, 35, 36]. Nevertheless, cubic kinetics were found to be a good match to the limited mass gain data available to us for

Table 3: Main parameters used in the oxidation simulations.

T (°C)	1150
t (h)	200
$V_{Al_2O_3}$ (cm^3/mol)[a]	25.6
$V_{Cr_2O_3}$ (cm^3/mol)[a]	29.1
V_a (cm^3/mol)[b]	7.2
n	3
k (m^3/s)	3×10^{-22}

[a] At room temperature [37]. Value varies with temperature but these variations are small compared to the uncertainty on k.
[b] Average for the compositions of interest at 1150 °C calculated with Thermo-Calc and TCNI8 (molar volumes are not available in CRALDAD).

these alloys at 1150 °C, and were therefore used in the simulations. The parameters used in the simulations are given in Table 3.

In the case of the thinner specimens, after some time, x_{Al}^{int} decreased to a value where the simulation could no longer proceed with the prescribed boundary condition, Eq. (3). At this stage, the boundary condition was changed and Cr_2O_3 growth was considered instead. This is presented in Section 4.

3 Results

3.1 Experimental results

Overview

Figure 4 shows photographs of the specimen surfaces throughout the 200 h experiment. The oxides can be identified based on their color: Al_2O_3 is grey/blue, Cr_2O_3 is dark green, while Ni- and Co-rich oxides are dark grey. All alloys were found to follow the same sequence of oxidation regimes. All specimens initially formed Al_2O_3 scales. The thicker specimens (A series, 400–500 µm) retained this behavior throughout the 200 h experiment, while some of the thinner specimens transitioned to less protective regimes. The duration of this first stage increased with increasing alloy thickness and Al concentration. A first transition was observed as Cr_2O_3 started to appear at the specimen edges, and with time progressed toward the center until it covered the whole surface. A second transition occurred in a similar manner, with Ni- and Co-rich oxides developing from the edges toward the center. On some specimens, the transitions started at the center, where pores due to the casting process were present. Finally, the thinnest specimens broke into pieces.

The thickest specimens of alloys UT11 and UT17 were subject to significant oxide spallation, visible from the light grey color in Fig. 4(a). These specimens remained flat throughout the experiment, whereas the thinner specimens, for which no spallation was observed, tended to deform.

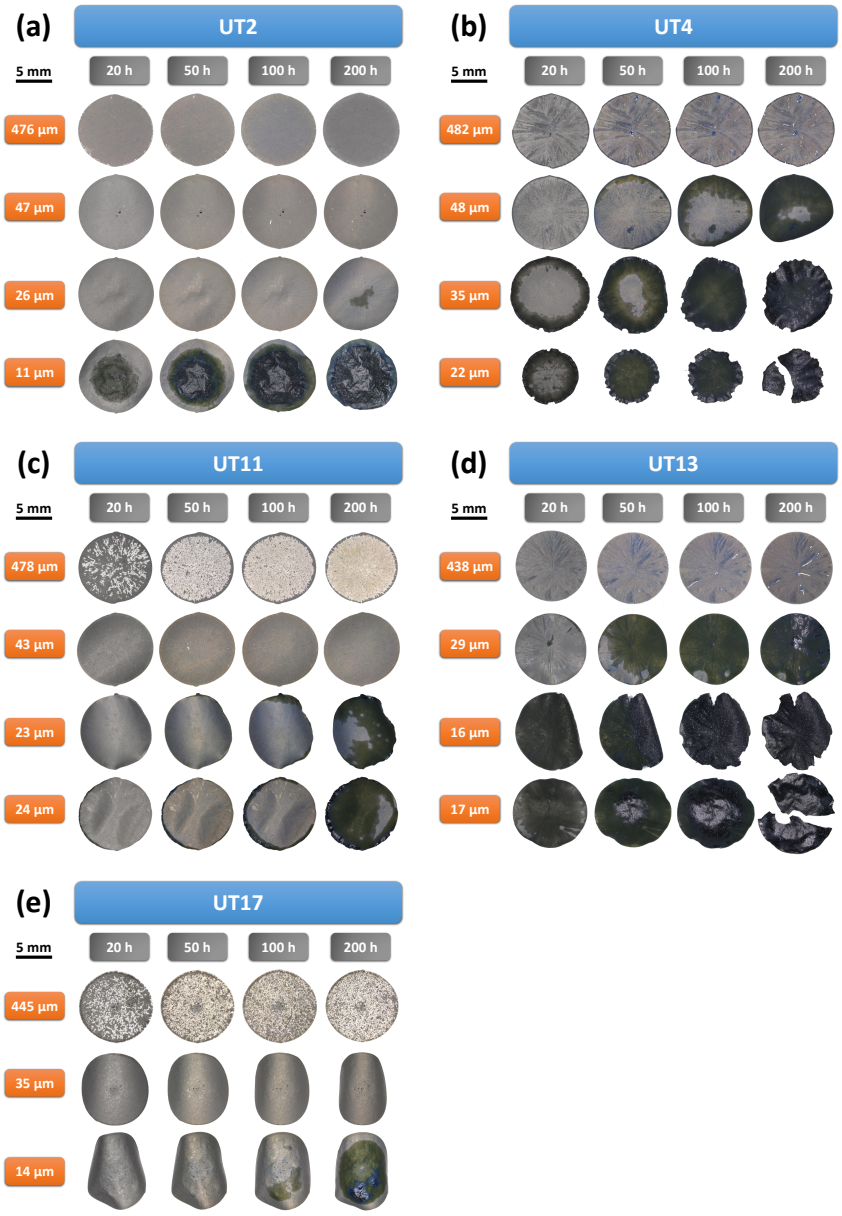

Figure 4: Photographs of the specimens at interruptions of the 1150 °C oxidation experiment. Grey/blue: Al_2O_3; dark green: Cr_2O_3; dark grey: Ni- and Co-rich oxides; light grey: alloy.

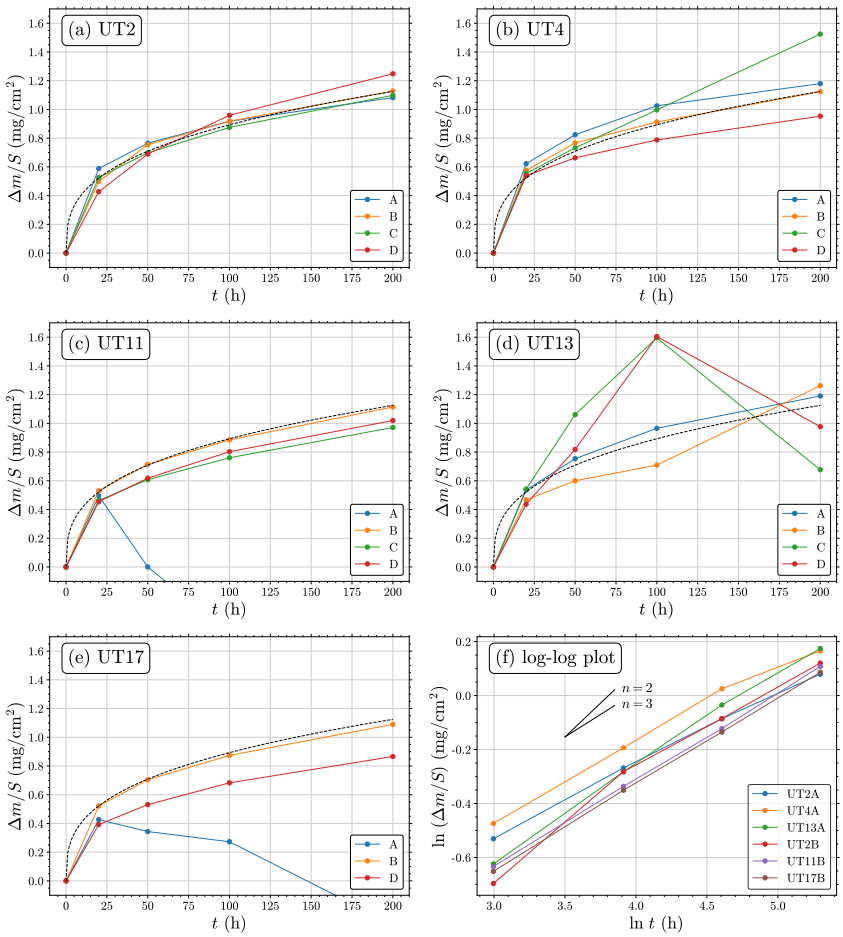

Figure 5: Mass changes recorded during oxidation at 1150 °C. In (a)-(e), the dashed line represents the mass gains corresponding to the growth of a pure Al_2O_3 scale according to the rate law chosen for the simulations, Eq. (1) and Table 3; (f) shows a log-log plot for the specimens that remained in the stage of Al_2O_3 growth throughout the 200 h.

The mass changes recorded at each interruption of the experiment are plotted in Fig. 5. The oxidation kinetics of all specimens in the Al_2O_3 growth stage are found to be similar. The transitions from Al_2O_3 to Cr_2O_3 and then to Ni- and Co-rich oxides, identified above from the photographs, caused the mass gain to slightly deviate from the trend set by Al_2O_3 growth. However, no specimen exhibited an abrupt acceleration. The small oxide pieces that broke out were not collected. This resulted in a mass loss (specimens UT4 and UT13). Likewise, the effect of oxide spallation on specimens UT11A and UT17A is manifested in an important mass loss.

A log-log representation of the mass change for the specimens that remained in the stage of Al_2O_3 growth throughout the 200 h experiment, shown in Fig. 5(f), was used to analyze Al_2O_3 growth kinetics. A linear function was fitted to each log-log series with a least-squares method. The slope was found to be 0.31 ± 0.03 (average $\pm$ standard deviation on the 6 specimens), which translates to $n = 3.2 \pm 0.3$ in the power rate law, Eq. (1). In previous work on the same alloys, Al_2O_3 growth was found to be

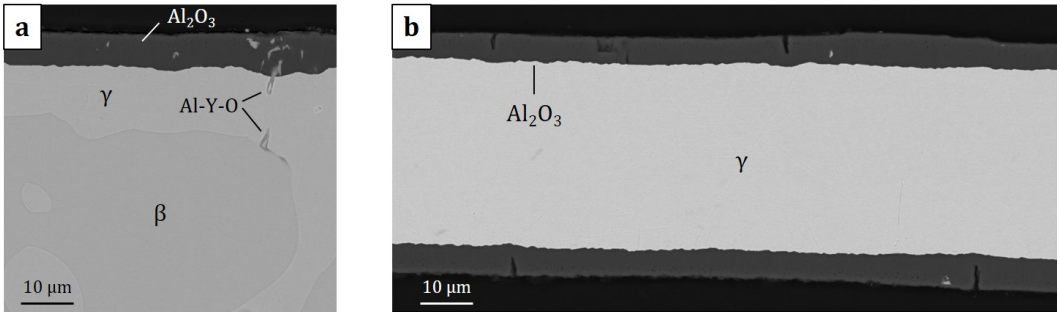

Figure 6: Cross-section SEM images of alloy UT2 after 200 h oxidation at 1150 °C. (a) UT2A (476 µm), (b) UT2B (47 µm).

faster above β regions than above γ regions in the first minutes of exposure, before the trend reversed, and differences faded after hundreds of hours [38]. Here, since the number of data points was small in each series, the differences observed between the specimens were deemed to be too small to constitute reliable measurements of an effect of alloy composition. We therefore decided to use the same n value for all specimens in the DICTRA simulations; the value $n = 3$ was picked out of simplicity. The data series were fitted again, this time with a fixed slope of 1/3 and only adjusting the intercept; this yielded the k value reported in Table 3. The mass gains calculated with these n and k values are shown as dashed lines in Fig. 5(a)-(e).

Reaction products

Analysis of the cross-sections by SEM–EDS showed that the thicker specimens behaved like their bulk counterparts [25, 38]: they formed Al_2O_3 scales, with mixed Al-Y oxide particles and occasionally transient spinel oxides at the surface. Furthermore, in the γ–β and β alloys, Al consumption to form the Al_2O_3 caused subsurface β dissolution: this is illustrated in Fig. 6(a).

In the thinner specimens, β dissolution extended across the whole thickness, as shown in Fig. 6(b). Among the specimens of the B series (35–50 µm), only those with more than 20 at. % Al (UT2, UT11 and UT17) were still exclusive Al_2O_3-formers at the end of the 200 h experiment. In these cases, the Al_2O_3 scale was similar to that formed on the thicker specimens, except that it presented transverse cracks, as seen in Fig. 6(b). Average scale thicknesses measured on the specimens that formed Al_2O_3 exclusively are gathered in Fig. 7. We note that the value obtained from the oxidation model used in the DICTRA simulations (power law adjusted to the mass gain data), shown as a dashed line, is close to the measured thicknesses.

The B series specimens with less than 20 at. % Al, as well as the thinner specimens, presented a wide variety of reaction morphologies. As mentioned earlier and seen in Fig. 4, the transitions between oxidation stages did not occur in a uniform manner on the specimen surfaces. Several stages were sometimes visible on a given specimen, depending on the local thickness and proximity with the edges and center (which acted as initiation sites). This is illustrated in Fig. 8 for specimen UT17D:

- in the thicker zones/away from initiation sites, a thin Cr_2O_3 layer is present between the alloy and the Al_2O_3 (Fig. 8(b));

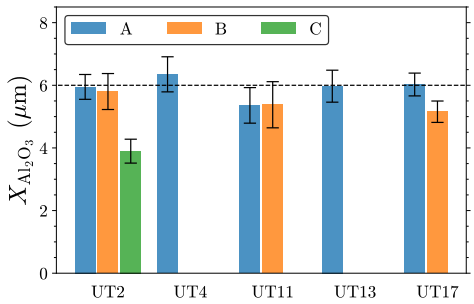

Figure 7: Average scale thickness measured on specimens that only formed Al_2O_3, after 200 h at 1150 °C. The dashed line shows the value corresponding to the boundary condition used in the DICTRA simulations.

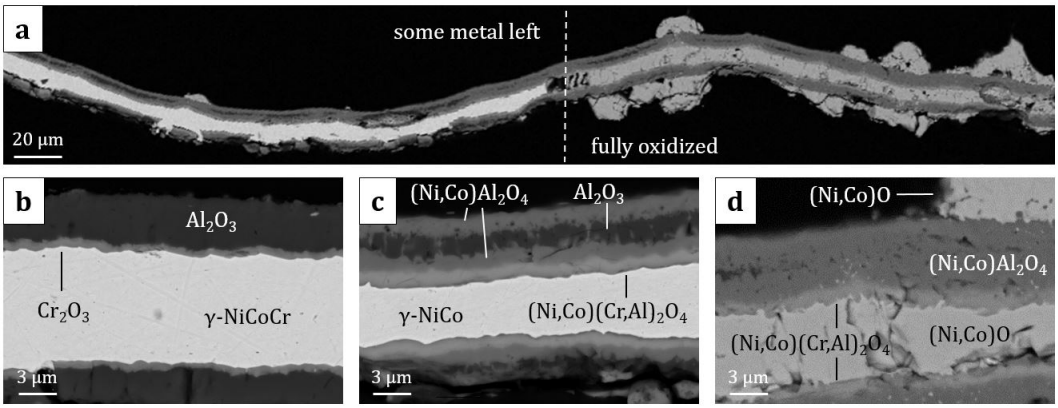

Figure 8: Cross-section SEM images of alloy UT17D (14 µm) after 200 h oxidation at 1150 °C, showing several stages of the oxidation process. (a) Overview, (b) Al_2O_3 and thin Cr_2O_3, (c) Ni and Co oxide around the Al_2O_3, and (d) alloy fully oxidized.

- in intermediate zones, mixed spinel oxide layers are present both underneath the Al_2O_3, replacing the Cr_2O_3, and at the scale surface (Fig. 8(c));
- in the thinner zones/close to initiation sites, the Al_2O_3 has been fully converted to spinel oxide, the alloy has been converted to (Ni,Co)O, and (Ni,Co)O particles are present at the scale surface (Fig. 8(d), see also right hand side of Fig. 8(a)).

This general sequence was observed for all five alloys, with minor variations in the oxide morphologies and compositions. In particular, the Cr_2O_3/Al_2O_3 interface was more or less sharp. In Figs. 9(a) and (c) for instance, there is a zone of intermediate contrast between the two layers, and the composition varies continuously between that of Cr_2O_3 (with $\sim$ 1–3 at. % Al) and that of Al_2O_3 (with no significant Cr). This composition gradient may reflect ongoing interdiffusion between the oxides, but it may also in part be the result of a measurement artifact, and reflect varying volume fractions of each oxide in the analyzed material, which is not necessarily uniform in the out-of-plane direction — indeed, Cr_2O_3 appears to be developing along Al_2O_3 grain boundaries, as observed by previous investigators [19, 20]. This is less apparent in other micrographs (see Figs. 8(b), 9(b) or 9(d) for instance),

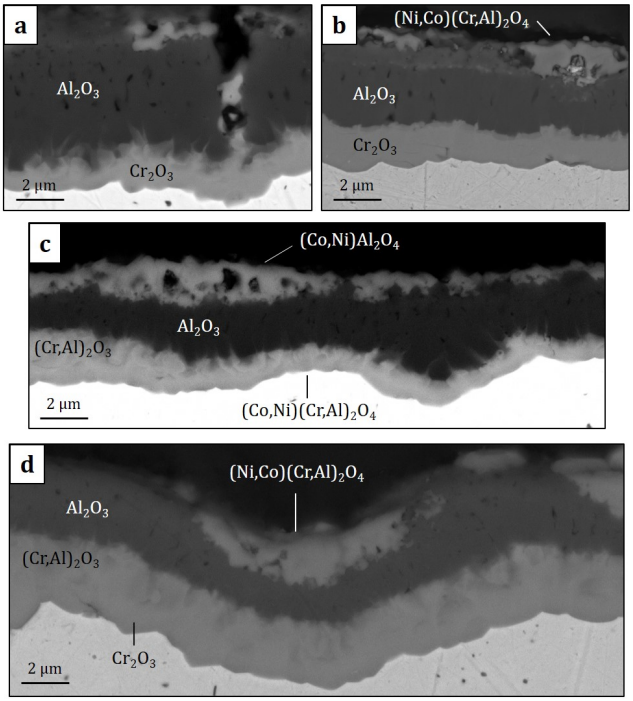

Figure 9: Cross-section SEM images of alloys (a) UT4B (48 µm), (b) UT13B (29 µm), (c) UT2D (11 µm) and (d) UT4C (35 µm) after 200 h oxidation at 1150 °C.

where the Cr_2O_3/Al_2O_3 interface appears to be sharp and the oxides are close to stoichiometric ($\sim$ 1–3 at. % Al in Cr_2O_3 and no significant Cr in Al_2O_3).

Another aspect of interest is that Cr_2O_3 layers grew to varying thicknesses before being converted to spinel, reflecting the variable amount of Cr available in the specimens. In Fig. 9(c), the lowermost layer is spinel oxide, whereas in Figs. 9(b) and (d), the lowermost layer is Cr_2O_3 and takes up a larger proportion of the total scale thickness. Variations were also observed in the spinel oxide composition; the latter reflected the initial composition of the alloys.

Alloy composition

Alloy compositions were measured by SEM–EDS. Figures 10 and 11 show the profiles recorded in the thicker specimens of the single-phase alloys, UT13A (γ) and UT17A (β), and of two γ–β alloys, UT2A and UT11A. After 200 h, all of these specimens are still in the Al_2O_3 growth stage, and their composition is still quite close to the nominal composition (indicated by dashed lines in Fig. 10). In particular, the β alloy remained fully β. Slight composition gradients are observed in the γ alloy (Fig. 10(a)), while no gradients are seen in the β alloy (Fig. 10(b)), or in either phase of the γ–β alloys (Fig. 11).

Figure 12 shows the profiles recorded in the specimens of the B and C series that were still in the Al_2O_3 growth stage after 200 h. Again the profiles are found to be essentially flat. However, the Al concentration decreased significantly, to a point where no β phase is left, even in the case of the (initially) full β alloy, UT17. In the thinner specimens, UT17B and UT2C, the composition was found to vary

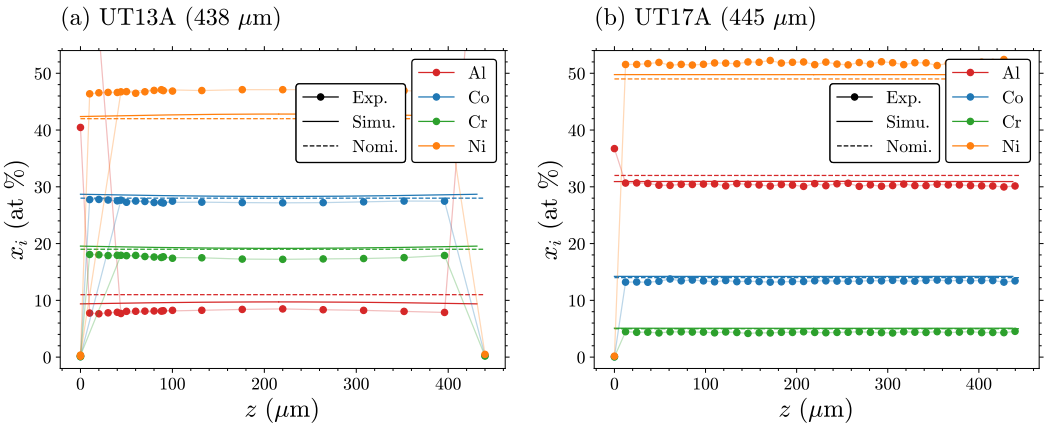

Figure 10: Experimental and simulated (DICTRA) concentration profiles for alloys (a) UT13A and (b) UT17A after 200 h at 1150 °C. Nominal concentrations added as dashed lines for reference.

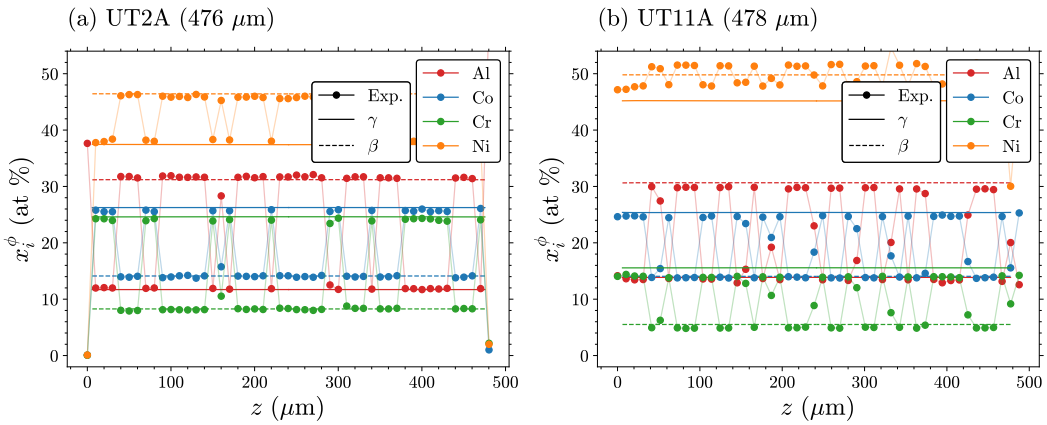

Figure 11: Experimental and simulated (DICTRA) concentration profiles for alloys (a) UT2A and (b) UT11A after 200 h at 1150 °C.

significantly from one place to another on the same cross-section. The variability is particularly pronounced in UT2C: in one location, the Al content is $\sim$ 2 at. %, indicating that the alloy is close to Al_2O_3 failure, whereas in the other location, there is still $\sim$ 10 at. % Al left, and the alloy is 7 µm thicker.

Figure 13 shows profiles recorded in specimens in the stage of Cr_2O_3 growth, a situation depicted in Figs. 8(b) and 9(a-b). Aluminum is seen to be fully exhausted, while the Cr concentration has significantly decreased, and varies significantly from one place to another. As in the other specimens, no gradient is observed in the profiles.

Profiles were also recorded in specimens where Ni and Co have started to oxidize, as in Figs. 8(c-d) and 9(c-d). In these cases, the remaining alloy was found to be free of both Al and Cr (not shown here).

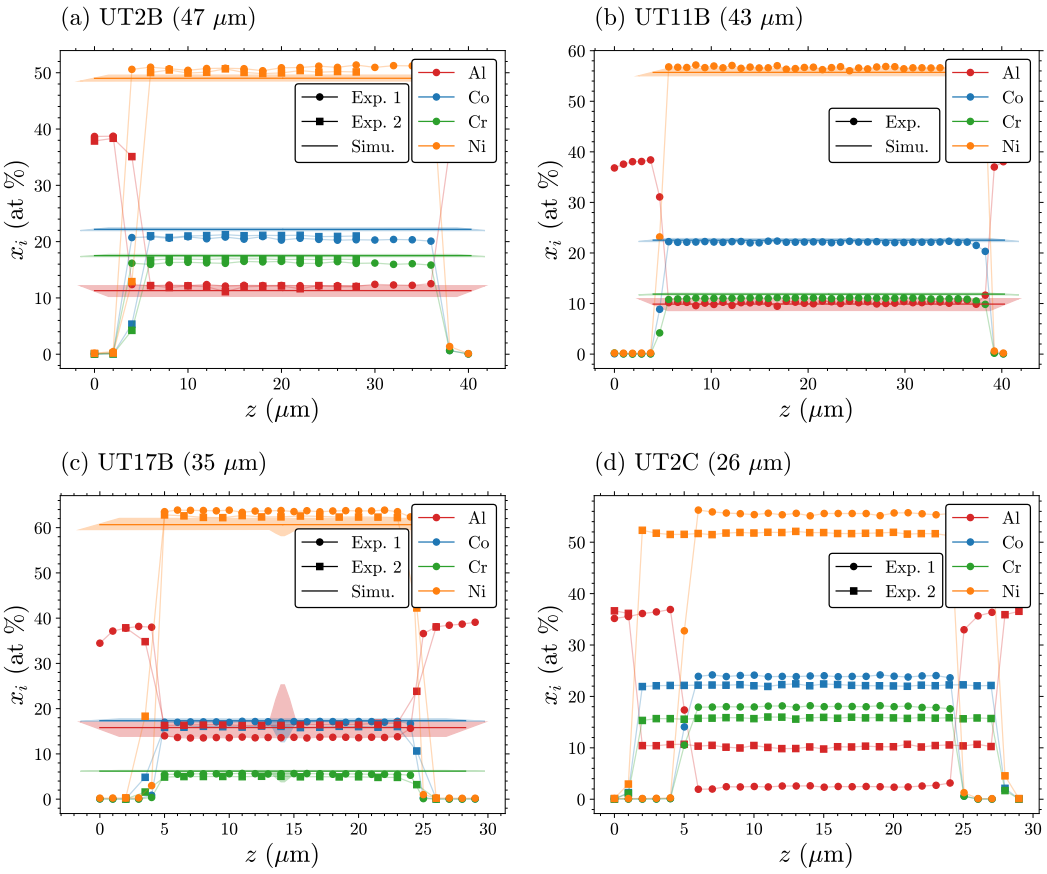

Figure 12: Experimental and simulated (DICTRA) concentration profiles for alloys (a) UT2B, (b) UT11B, (c) UT17B and (d) UT2C after 200 h at 1150 °C. The lower and upper limits of the shaded bands represent profiles simulated with an initial alloy thickness at – and + 3 µm, respectively, of the average. The shape taken by the shaded band in (c) is due to the fact that some β phase was left in the specimen center in the + 3 µm simulation. In (d), the simulation run with the average initial thickness resulted in full Al consumption before 200 h.

3.2 Simulation results

Alloy composition profiles in the Al_2O_3 growth regime

The composition profiles obtained from the DICTRA simulations in the Al_2O_3 growth regime are compared with the experimental results in Figs. 10–12. The effect of the initial alloy thickness was studied by performing simulations with values representative of the experimental variations, i.e., at + and – 3 µm of the average thickness. These variations made no significant difference in the thicker specimens (A series). In thinner specimens, however, they had a visible impact on the profiles, and in particular on the Al concentration. This is represented by shaded bands in the profiles of Fig. 12.

In the thicker specimens, the agreement between simulated and measured profiles is found to be excellent, as the difference is typically below 1 at. %, i.e., within experimental uncertainty (Figs. 10 and 11).

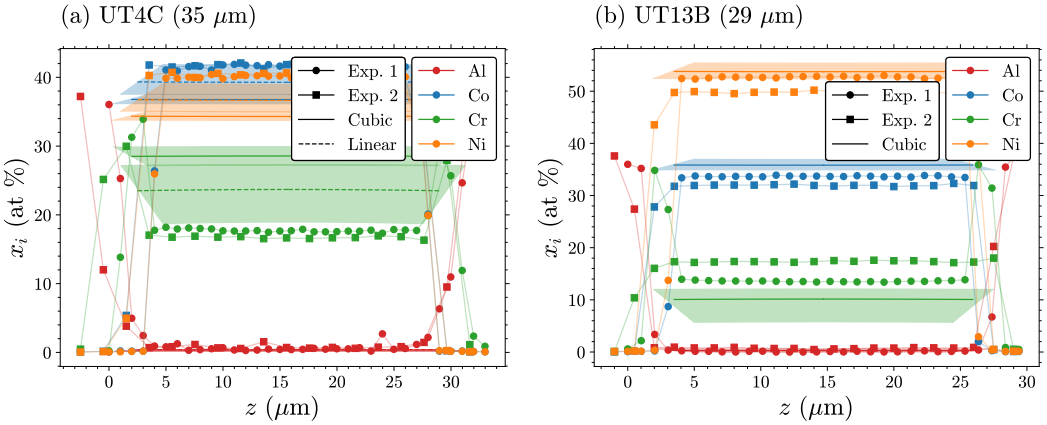

Figure 13: Experimental and simulated (DICTRA) concentration profiles for alloys (a) UT4C and (b) UT13B after 200 h at 1150 °C. Simulated profiles obtained with either cubic or linear Cr_2O_3 growth kinetics — see text for details. In (b), linear kinetics led to full Cr consumption before the end of the 200 h simulation.

In the thinner specimens, the experimental profiles fall within the band defined by the ± 3 µm simulations (Fig. 12). One exception to this generally good agreement is observed in specimen UT2C. Using the measured average value of 26 µm as initial alloy thickness, the simulation predicted that Al would be completely exhausted after 170 h. Experimentally, Cr_2O_3 started to appear at the specimen center between 100 and 200 h (Fig. 4), but most of the specimen was still Al_2O_3-former after 200 h. In these regions, the remaining Al concentration in the alloy was highly variable (Fig. 12(d)) — more than expected from the initial thickness variation. This specimen presented another peculiarity: the Al_2O_3 scale was significantly thinner than that formed on the other specimens, ∼ 4 µm instead of ∼ 6 µm (Fig. 7). The reason for this discrepancy is not known, but the lower scale thickness would certainly be associated with a lesser Al consumption; this qualitatively explains why Al_2O_3 remained stable for a longer time, and more Al was left in the alloy, than simulated.

3.3 Alloy phase transformations in the Al_2O_3 growth regime

The DICTRA simulations describe the evolution of phase compositions and fractions over time. This is now exploited to examine the phase transformations caused by the selective oxidation of Al. The analysis of the simulated profiles shows that for the γ–β alloys, the Al removal due to Al_2O_3 growth is mainly accommodated by the complete dissolution of β in a subsurface zone, while in the rest of the alloy, the volume fraction of β (f_β) slightly decreases. This defines a distinct β dissolution front. The composition on either side of this front is all but uniform. This is illustrated in Fig. 14, where the Al and β fraction profiles are plotted at 50 and 200 h for a thick specimen, UT2A. Note that in the γ–β zone, the decrease in f_β results in a slight decrease of the overall Al fraction, but also has the counterintuitive consequence of increasing the Al fraction in γ. This is simply due to the topology of the phase diagram. Overall, these phase composition changes are small, and the main consequence of Al consumption is the progression of the β dissolution front.

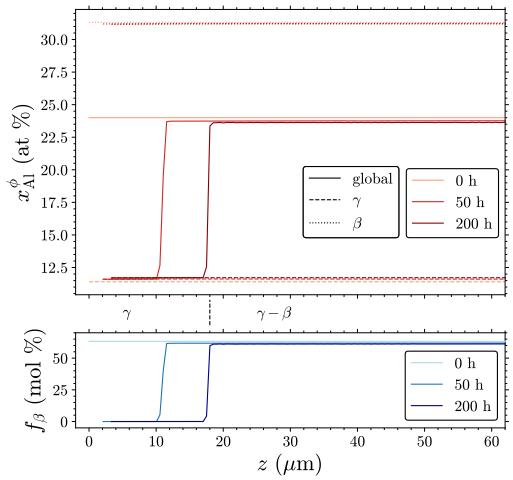

Figure 14: Simulated (DICTRA) Al and β fraction profiles at 0, 50 and 200 h in alloy UT2A.

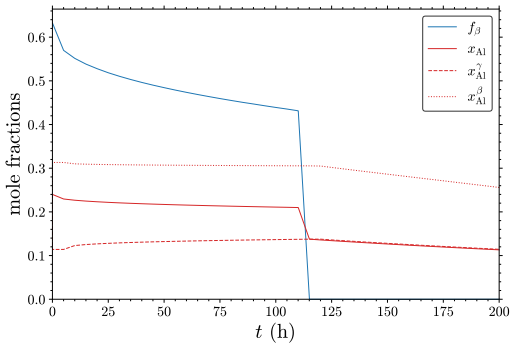

Figure 15: Simulated (DICTRA) time evolution of Al and β fraction at mid-specimen in alloy UT2B during oxidation at 1150 °C.

In thin specimens, the β dissolution eventually reaches the specimen center, at which point the alloy becomes single-phase γ. This is illustrated in Fig. 15, which shows the time evolution of f_β at mid-specimen in UT2B: f_β gradually decreases during 113 h, and then drops to 0. This transition time was extracted from all simulations, and is plotted as a function of initial alloy composition and thickness in Fig. 16. The thickness dependence follows a plain power law. As shown in the Discussion, because of the fast alloy diffusion, the time-to-β dissolution can be related to the oxidation kinetics via an analytical expression.

Time-to-Al_2O_3 failure

Alumina fails when $x^{\text{int}}_{\text{Al}}$, the Al fraction at the alloy/scale interface, reaches x^{*}_{Al}, the Al content at Al_2O_3–Cr_2O_3 equilibrium. As noted in Section 3.1, wherever Cr_2O_3 was observed at the base of the scale, no significant Al was found in the alloy. We will show in the Discussion that x^{*}_{Al} is indeed very small and can be approximated as 0. The time-to-Al_2O_3 failure, t_f, is then simply obtained as the time when $x^{\text{int}}_{\text{Al}}$ reaches 0 in the simulation. This also corresponds to the time when the boundary

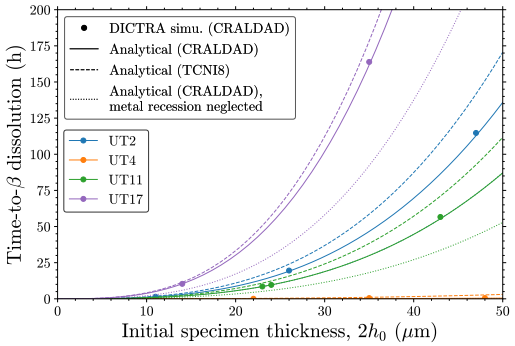

Figure 16: Time to β dissolution determined from the DICTRA simulations. Also included are the results from the analytical solution, Eq. (8), where the threshold Al fraction for β stability was calculated using either CRALDAD or TCNI8, and the results obtained by further neglecting the metal recession, Eq. (10) (see text for details).

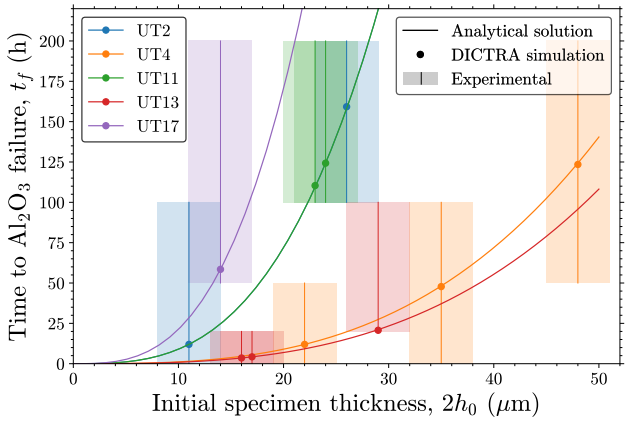

Figure 17: Time to Al_2O_3 failure determined from the DICTRA simulations and the analytical solution, Eq. (11). Experimental values are also given, as intervals determined by visually inspecting the specimens at each interruption. The shaded rectangles are defined by these intervals and a ± 3 µm range around the average initial specimen thickness.

condition, Eq. (3), can no longer be fulfilled, and the simulation stops. Values of t_f thus obtained are plotted in Figure 17.

Experimentally, Al_2O_3 failure did not occur uniformly over the specimen surfaces (Fig. 4). Lower and upper bounds of t_f were estimated by visually inspecting the specimens after each interruption, excluding the edges. These are included in Fig. 17 for comparison. Qualitatively, the composition and thickness dependence of the time-to-failure observed experimentally is correctly reproduced in the simulations. However, the spread observed experimentally within a given specimen is generally larger than the spread expected from the simulations, considering variations of ± 3 µm in the initial specimen thickness.

Like the time-to-β dissolution, the time-to-failure follows a simple power law. The analytical expressions are derived in the next Section.

4 Discussion

The discussion will first consider the stage of Al_2O_3 growth. We will show that for a large part, the alloy response to oxidation can be described analytically using the approximation of uniform alloy composition. The effect of the problem parameters is readily examined with the analytical treatment; this will be used to study the influence of the thermodynamics database used in calculating metrics relevant to multiphase alloys, the effect of neglecting the metal recession in thin specimens, and the sensitivity of the alloy response to its initial thickness. The discussion will then turn to the thermodynamic and mechanistic aspects involved in the transition from Al_2O_3 to Cr_2O_3, spinel oxide and (Ni,Co)O growth. Finally, we will present an attempt at modelling Cr_2O_3 growth after Al_2O_3 failure.

4.1 Approximation of flat depletion profiles

The composition profiles measured in all specimens were found to be essentially flat. This reflects the fact that diffusion was fast in both γ and β, relative to the oxidation rate. With the assumption of flat profiles, calculating the time evolution of an alloy composition reduces to a 0-dimension problem, which can be solved analytically. In the Al_2O_3 growth stage, the quantity of each of Co, Cr and Ni remains constant; making the approximation of a constant alloy molar volume and neglecting creep, this can be expressed as

$$\frac{x_i}{x_i^0} = \frac{h_0}{h}, \qquad i = \mathrm{Co, Cr, Ni}, \tag{4}$$

where x_i is the atom fraction of species i, h the specimen half-thickness, and 0 used as subscript or superscript indicates values at $t = 0$. It follows that

$$\frac{1 - x_{\mathrm{Al}}}{1 - x_{\mathrm{Al}}^0} = \frac{h_0}{h}. \tag{5}$$

The specimen half thickness h is related to the scale thickness by the relation [4]

$$\frac{h_0 - h}{V_{\mathrm{a}}} = \frac{2X_{\mathrm{Al_2O_3}}}{V_{\mathrm{Al_2O_3}}}. \tag{6}$$

If the time evolution of $X_{\mathrm{Al_2O_3}}$ is known, the alloy composition can then be calculated from Eqs. (4) and (5). In particular, with power law kinetics, Eq. (1), the Al fraction is given by:

$$x_{\mathrm{Al}} = 1 - \frac{1 - x_{\mathrm{Al}}^0}{1 - \dfrac{2V_{\mathrm{a}}}{V_{\mathrm{Al_2O_3}}} \dfrac{(k \cdot t)^{1/n}}{h_0}}. \tag{7}$$

Values corresponding to the alloys of interest were calculated using the parameters used in the simulations (Table 3); these are not included in Figs. 10–13 for the sake of readability, but they were found to be in close agreement with the simulated profiles. In the case of two-phase alloys, the x_i values given by Eqs. (4) and (5) are to be compared with global concentrations, which are not shown in Figs. 10–12 but are accessible from the DICTRA simulations.

Rearranging Eqs. (1), (4), (5) and (6), the time needed to reach a given x_{Al} value can be calculated as:

$$t = \frac{1}{k}\left(\frac{V_{\mathrm{Al_2O_3}}}{2V_{\mathrm{a}}} \cdot h_0 \cdot \frac{x^0_{\mathrm{Al}} - x_{\mathrm{Al}}}{1 - x_{\mathrm{Al}}}\right)^n . \tag{8}$$

We note that Eq. (8) is slightly different from the expression given by Quadakkers and Bongartz [7] and used by other investigators [11]. The latter makes the approximation that the metal recession is small compared to the initial alloy thickness and can be neglected, i.e., that $h \approx h_0$. This becomes apparent when writing that the amount of Al in the scale equals that consumed in the alloy:

$$\frac{X_{\mathrm{Al_2O_3}}}{V_{\mathrm{Al_2O_3}}} = \frac{1}{2V_{\mathrm{a}}}\left(h_0 \cdot x^0_{\mathrm{Al}} - h \cdot x_{\mathrm{Al}}\right). \tag{9}$$

Equation (9) is equivalent to Eq. (8), but yields the commonly used expression if $h = h_0$:

$$\frac{X_{\mathrm{Al_2O_3}}}{V_{\mathrm{Al_2O_3}}} = \frac{1}{2V_{\mathrm{a}}} h_0 \left(x^0_{\mathrm{Al}} - x_{\mathrm{Al}}\right). \tag{10}$$

We further note that the relative error made in using Eq. (10) does not in fact depend on the initial alloy thickness. Indeed, x_{Al} and h are related, by virtue of Eq. (5): if the specimen is so thick that $h \approx h_0$, then x_{Al} cannot be much smaller than x^0_{Al}. The approximation only becomes valid when the target concentration x_{Al} is close to 0: if the remaining metal contains little Al, the remaining thickness has little influence — this is also apparent in Eq. (9).

The time to Al_2O_3 failure is obtained by setting $x_{\mathrm{Al}} = 0$ in Eq. (8):

$$t_f = \frac{1}{k}\left(\frac{V_{\mathrm{Al_2O_3}}}{2V_{\mathrm{a}}} \cdot h_0 \cdot x^0_{\mathrm{Al}}\right)^n . \tag{11}$$

Values of t_f calculated with Eq. (11) are plotted alongside those determined from the DICTRA simulations in Fig. 17. The two sets of results are in agreement, which confirms that the approximation of fast alloy diffusion is justified here. We also note that insofar as this approximation applies, the time-to-failure obtained from DICTRA simulations does not depend on the databases used to perform the simulations, since t_f simply reflects the total amount of Al initially present in a given specimen.

Another time of interest is that required to fully consume the β phase. The threshold x_{Al} value can be determined by varying the amount of Al (number of moles) while keeping the amounts of Ni, Co and Cr constant, as would happen when an alloy loses Al by oxidation, and finding the value where f_β reaches 0, i.e., the $\gamma + \beta$ / γ equilibrium. This was done using Thermo-Calc and the CRALDAD database. For instance, we obtained $x_{\mathrm{Al}} = 13.8$ at. % in alloy UT2. The time to β dissolution was then calculated with Eq. (8); this is plotted as a function of the initial specimen thickness for the alloys of interest in Fig. 16 (alloy UT13 is not included because it contains no β phase at 1150 °C). This analytical model is seen to be consistent with the values obtained from the DICTRA simulations.

Contrary to the time-to-failure, the time-to-β dissolution relies on a phase equilibrium; the calculated value therefore depends on the thermodynamics database

that was used to compute this equilibrium. The above calculation was repeated using the TCNI8 database: we obtained $x_{\mathrm{Al}} = 12.8$ at. % for the threshold Al fraction in the UT2 alloy. This is ~ 1 at. % lower than the CRALDAD calculation, which translates into a slightly longer time-to-β dissolution. The same trend was obtained for the other alloys. The corresponding times are compared to those obtained with CRALDAD in Fig. 16. The difference between the results obtained with the two databases is 26 %, 28 % and 10 % for alloys UT2, UT11 and UT17, respectively.

Figure 16 also includes the values obtained with CRALDAD but neglecting the metal recession, i.e., using Eq. (10). Making this approximation reduces the time-to-β dissolution by 36 %, 39 % and 43 % for alloys UT2, UT11 and UT17, respectively.

The expression obtained in the approximation of fast alloy diffusion, Eq. (8), has the advantage of exposing the influence of the problem parameters in a straightforward manner. If the oxidation constant k is multiplied by 10, for instance, the time-to-β dissolution will be divided by 10. When this approximation is not valid (at lower temperatures), the influence of the parameter can still be studied analytically when an analytical solution of the problem exists, i.e., in a pseudo-binary, single-phase system with composition-independent interdiffusion coefficient, following purely parabolic kinetics and neglecting the metal recession: this was done by Young et al. [39]. In the more general case of a multicomponent, multiphase alloy of any thickness and oxidation rate law, useful metrics can only be obtained from numerical simulations of alloy diffusion such as those conducted in the present work or by previous investigators, see for instance Refs [40, 41, 42, 43, 44, 45].

4.2 Validity and limits of the simulations

In the Al_2O_3 growth stage, the simulations were conducted under the assumption of cubic oxidation kinetics with an alloy-independent k, a drastic simplification of what is in fact a complex process. Nevertheless, the resulting profiles were found to match the measured compositions within experimental uncertainty.

We note that since alloy diffusion was fast relative to the rate of Al removal, the alloy composition was not very sensitive to the oxidation model: a different exponent in Eq. (1), or another rate law altogether, would have produced similar composition profiles so long as the final Al_2O_3 thickness was the same. In this regard, the good agreement between experimental and simulated profiles at one point in time does not in itself demonstrate that the time-evolution of Al_2O_3 growth was suitably described — this was instead shown by the time-dependent mass gain data. Nevertheless, it does indicate that the underlying mass balance, as well as the alloy phase equilibria and diffusion process, were correctly modeled.

In other words, given a rate law, the consequences of Al_2O_3 growth on the composition of a perfectly uniform γ–β NiCoCrAl specimen can be correctly simulated. Of course, actual specimens inevitably include imperfections (metallurgical defects such as pores or oxide inclusions, surface preparation defects, thickness variations). The effects of these imperfections on oxidation-induced composition changes are stronger in thinner specimens. This follows from Eqs. (4) and (5), and with regards to thickness variations, it is manifested in Figs. 10–13 by the fact that the shaded bands representing profiles calculated at $2h_0 \pm 3$ µm are wider in thinner specimens.

An aspect which has been neglected emerges from the comparison of experimental and simulated profiles in Figs. 12 and 13: after 200 h, the reacted alloys were

consistently thinner than expected from the mass balance underlying oxidation. This thickness reduction is believed to be due to creep, as observed in other studies of thin foils oxidized at high temperature [16]. The occurrence of creep can have complex implications with regard to the alloy response to oxidation, for a number of reasons related to the interactions between stress and alloy diffusion [46]. These effects would be expected to be more pronounced in thinner specimens, as those would have larger creep rates. The comparison between experimental and simulated profiles suggests that creep-related effects were not pronounced in specimens above ~ 30 µm; no conclusion can be drawn in the case of thinner specimens. A more detailed account of oxidation-creep interactions cannot be arrived at from the present results.

4.3 Reaction mechanism

The Discussion now turns to the thermodynamic and mechanistic aspects of the transitions between the oxidation regimes observed here, from Al_2O_3 scaling to full metal consumption. All thermodynamic calculations were done using Thermo-Calc, with the TCNI8 database (oxides are not included in CRALDAD).

During Al_2O_3 growth, once a steady-state is established, the p_{O_2} at the alloy/scale interface is controlled by the $\underline{Al}$–Al_2O_3 equilibrium, where $\underline{Al}$ designates Al in solution in the alloy. Assuming that the Al_2O_3 activity is one, this can be expressed as

$$\frac{1}{a_{Al}^2 p_{O_2}^{3/2}} = \exp\left(-\frac{\Delta_f G_{13}^0}{RT}\right), \tag{12}$$

where a_{Al} is the activity of Al in the alloy solution and $\Delta_f G_{13}^0$ is the standard free energy of formation of Al_2O_3 from pure Al in its reference state at the temperature of interest:

$$2Al\ (liq.) + \frac{3}{2}O_2\ (g) = Al_2O_3, \tag{13}$$

The conditions for Al–Al_2O_3 equilibrium and Al dissolution in the alloy at 1150 °C were calculated using the nominal composition of alloy UT2; one obtains $a_{Al} = 3.2 \times 10^{-4}$ (with reference to liquid Al) and $p_{O_2} = 5.9 \times 10^{-26}$ bar. As Al is consumed, a_{Al} decreases and p_{O_2} rises by virtue of Eq. (12) until Cr can be oxidized and reduce the Al_2O_3. This is represented in the predominance diagram of Fig. 18(a).

According to the thermodynamic assessment by Saltykov et al. [47], Al_2O_3 and Cr_2O_3 are completely miscible above ~ 930 °C at $p_{O_2} = 0.21$ bar, and would therefore be expected to form a corundum solution in the present case. The Cr content of the corundum would then gradually increase as the p_{O_2} increases. Instead, we observed separate Al_2O_3 and Cr_2O_3 layers with limited mutual solubility (Section 3.1). As pointed out by Chyrkin et al. [20], this is due to the relatively slow diffusion kinetics of Al and Cr in Al_2O_3. As Cr enters the Al_2O_3, it locally saturates it and Cr_2O_3 precipitates; the two layers tend to mix by interdiffusion, but slowlier than new Cr_2O_3 forms.

This metastable state implies that the conditions at which Cr_2O_3 precipitates can be calculated by considering the following displacement equilibrium:

$$Al_2O_3 + 2\underline{Cr} = Cr_2O_3 + 2\underline{Al}, \tag{14}$$

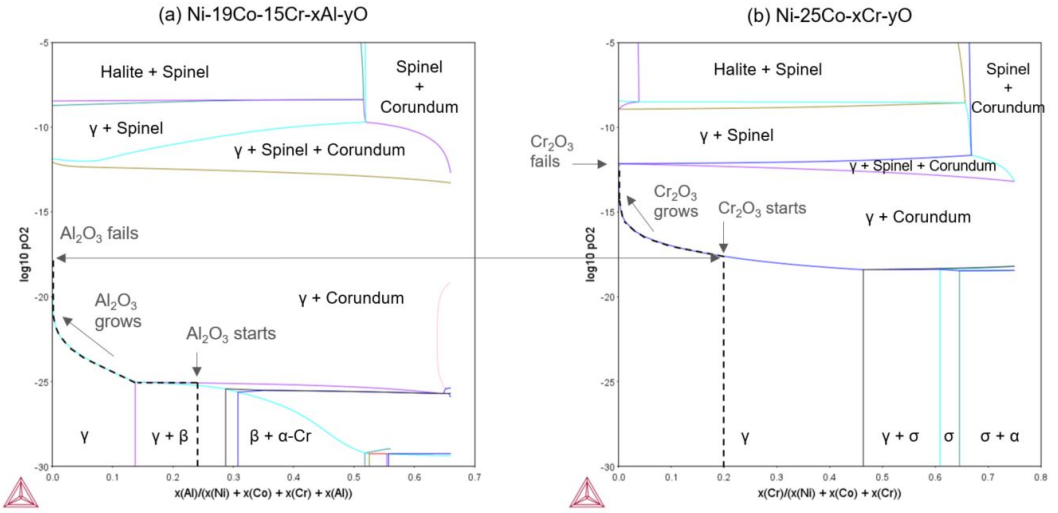

Figure 18: Predominance diagrams in the (a) Ni–Co–Cr–Al–O and (b) Ni–Co–Cr–O systems at 1150 °C, calculated with Thermo-Calc and the TCNI8 and TCOX10 databases. The dashed lines describe the evolution of the thermodynamic conditions at the alloy–scale interface during the oxidation of an alloy of initial composition UT2, during (a) Al_2O_3 and then (b) Cr_2O_3 growth (the composition at the start of Cr_2O_3 growth, Ni–25Co–20Cr, corresponds to a Ni–19Co–15Cr–24Al alloy that lost all of its Al).

where each oxide is assumed to be pure. The Al and Cr activities then verify

$$\left(\frac{a_{\mathrm{Al}}}{a_{\mathrm{Cr}}}\right)^2 = \exp\left(-\frac{\Delta_{\mathrm{f}}G^0_{14}}{RT}\right), \tag{15}$$

where $\Delta_{\mathrm{r}}G^0_{14}$ is given by

$$\Delta_{\mathrm{r}}G^0_{14} = \Delta_{\mathrm{f}}G^0_{17} - \Delta_{\mathrm{f}}G^0_{13}, \tag{16}$$

and $\Delta_{\mathrm{f}}G^0_{17}$ is the standard free energy of formation of Cr_2O_3 from pure Cr in its reference state at the temperature of interest:

$$2\mathrm{Cr}\ (\mathrm{bcc}) + \frac{3}{2}\mathrm{O_2}\ (\mathrm{g}) = \mathrm{Cr_2O_3}. \tag{17}$$

The values of $\Delta_{\mathrm{f}}G^0_{13}$ and $\Delta_{\mathrm{f}}G^0_{17}$ at 1150 °C were used with Eqs (16) and (15) to determine the $a_{\mathrm{Al}}/a_{\mathrm{Cr}}$ ratio at equilibrium. The dissolution equilibrium of Al and Cr was then calculated to obtain the Al atom fraction corresponding to this $a_{\mathrm{Al}}/a_{\mathrm{Cr}}$ ratio in a Ni–25Co–20Cr–xAl alloy (the Co and Cr concentrations correspond to alloy UT2 without the Al). This resulted in $x^*_{\mathrm{Al}} = 2.3\times10^{-4}$ at. %. This value is small and justifies the assumption made in Section 3.2 when determining the time-to-failure t_f ($x^*_{\mathrm{Al}} \approx 0$). The p_{O_2} corresponding to the alloy–Al_2O_3–Cr_2O_3 equilibrium is calculated to be 2.4×10^{-18} bar.

After Al_2O_3 failure, the Cr_2O_3 layer develops at the base of the scale and Cr diffuses into the remnant Al_2O_3 layer. As long as Cr_2O_3 grows, the p_{O_2} at the alloy/scale interface is controlled by the Cr–Cr_2O_3 equilibrium, and it is too low for Ni- and Co-containing spinel to form. Patches of spinel oxide were locally observed at the top of the scale (Fig. 9(a), (b) and (d)). These may have been formed at

the very start of the exposure, or after one of the interruptions. As suggested by Chyrkin et al. [20], thermal cycling produces cracks in the scale; upon heating up, if a crack exposes the alloy to the gas, transient Ni and Co oxide may form, and be pushed upwards as Al_2O_3 or Cr_2O_3 regrows. In addition, even if pure spinel oxide would not form below the Cr_2O_3, minute amounts of Ni and Co may dissolve in the corundum phase, and grain boundary diffusion would then produce a significant flux of these elements toward the surface, where the higher p_{O_2} would cause spinel to precipitate.

As Cr_2O_3 grows and consumes Cr, a situation analog to that of Al_2O_3 failure develops: a_{Cr} decreases, the p_{O_2} rises by virtue of the $\underline{Cr}$–Cr_2O_3 equilibrium, until Ni and Co can reduce the Cr_2O_3 (which, as a result of interdiffusion, now contains significant Al) and form spinel oxide by the displacement reaction:

$$(\underline{Ni}, \underline{Co}) + (Cr, Al)_2O_3 + \frac{1}{2}O_2 = (Ni, Co)(Cr, Al)_2O_4 \tag{18}$$

This is represented in the predominance diagram of Fig. 18(b). The threshold x_{Cr} and p_{O_2} values are determined by considering the alloy–corundum–spinel equilibrium; one obtains $x^*_{Cr} = 3.6 \times 10^{-3}$ at. % and $p_{O_2} = 7.0 \times 10^{-13}$ bar for an alloy of initial composition UT2 (now almost emptied of its Al and Cr) at 1150 °C. Like Al_2O_3, Cr_2O_3 fails at a Cr content that is below the EDS detection limit.

Reaction (18) produces the continuous layer observed at the base of the scale in Figs. 8(c) and 9(c). Their activity gradient across the scale, as well as the opposite p_{O_2} gradient, drive Ni and Co diffusion into the remnant Al_2O_3. Grain boundary diffusion produces a large Ni and Co flux without significantly affecting the composition of the Al_2O_3; as a result, Ni and Co accumulate the the scale/gas interface and another continuous spinel layer develops there (Figs. 8(c) and 9(c)), by a displacement reaction analog to reaction (18) but involving the remnant Al_2O_3 rather than the basal $(Cr, Al)_2O_3$. As bulk diffusion of Ni, Co and Cr proceeds from its grain boundaries and lower and upper surfaces, the remnant Al_2O_3 layer is converted to spinel and finally disappears (Fig. 8(d)).

In the stage of spinel oxide growth, the alloy reduces to a Ni–Co solution, and therefore the consumption of Ni and Co does not lead to a decrease of their activity. The p_{O_2} then remains at a value controlled by the alloy-spinel equilibrium, and is too large for the monoxide (Ni,Co)O to form. However, once Al_2O_3 is entirely converted, in the absence of available Al or Cr, Ni and Co saturate the spinel, the p_{O_2} rises and the monoxide is formed. As shown in Fig. 8(d), its fast growth converts the alloy in place, while nodules of (Ni,Co)O are also found above the scale surface. These have likely been pushed through cracks of the scale as a result of the volume change accompanying the alloy conversion.

As discussed in Section 4.4, after Al_2O_3 fails and stops growing, its presence as a continuous layer limits the growth of the Cr_2O_3 and spinel layers. When, in the last stage of the oxidation process, (Ni,Co)O finally forms, only a small amount of Ni–Co alloy is left to oxidize. As a result, the stages following Al_2O_3 failure are not accompanied by a strong increase of the mass gain: no breakaway is observed in Fig. 5.

4.4 Chromia growth

A difficulty in modeling the oxidation kinetics in the stage of Cr_2O_3 growth arises from the lack of direct experimental data: when considering the Cr_2O_3 layer at any given location of a specimen, we do not know for how long it has been growing, since the time to Al_2O_3 failure varies within each specimen. In the absence of time-dependent thickness measurements, or mass gain data reflecting the Cr_2O_3 layer alone, a Cr_2O_3 growth model cannot be built from an empirical rate law and instead requires assumptions.

From the observed t_f ranges and calculated t_f values (Fig. 17), Cr_2O_3 growth appears to have been much slower than it would have been in the absence of an Al_2O_3 layer at this temperature. Indeed, considering parabolic growth kinetics ($X^2_{Cr_2O_3} = k \cdot t$) with $k = 10^{-15}$ m^2/s at 1150 °C [48], a Cr_2O_3 scale would be 10–25 µm in the time range of interest, which is much thicker than observed here.

As discussed in Section 4.3, Cr_2O_3 starts forming when the p_{O_2} at the alloy/scale interface reaches 2.4×10^{-18} bar. As the Cr_2O_3 layer grows, the p_{O_2} at the Al_2O_3–Cr_2O_3 interface is no longer bounded by the equilibrium with the alloy, and presumably increases to ease the p_{O_2} gradient across the Al_2O_3 layer. The rate at which this occurs is not known, but at least in the beginning of its growth, the Cr_2O_3 layer is subject to a much smaller p_{O_2} gradient than it would in the absence of the Al_2O_3; this would contribute to its slower growth.

The defect structure of Cr_2O_3 is not fully understood, and is known to be system-dependent [1]. Kofstad [49] reviewed early data and concluded that outward Cr diffusion was predominant, via Cr interstitials at low p_{O_2} and Cr vacancies at high p_{O_2}. More recent work on pure Cr and Ni–30Cr [50, 51] concluded that Cr_2O_3 grew outward with Cr vacancies as the major defect at high p_{O_2}, and inward with O vacancies as the major defect at low p_{O_2}. In the present case, the p_{O_2} at the Al_2O_3–Cr_2O_3 interface is not known and likely varies over time, and the Cr_2O_3 contains some Al and likely trace amounts of Ni and Co. In the absence of specific information, two possibilities suggested by Strehl et al. [16] were considered:

- Cr_2O_3 grows predominantly by outward Cr diffusion. The rate-limiting step is O diffusion across the remnant Al_2O_3 layer, which can be modeled by

$$\frac{\mathrm{d}X_{Cr_2O_3}}{\mathrm{d}t} = \left(\frac{\mathrm{d}X_{Al_2O_3}}{\mathrm{d}t}\right)_{t=t_f^-}, \tag{19}$$

  where $t = t_f^-$ indicates that the derivative is taken immediately before t_f, i.e., using Eq. (1). One obtains:

$$\left(\frac{\mathrm{d}X_{Al_2O_3}}{\mathrm{d}t}\right)_{t=t_f^-} = \frac{k}{n}(k \cdot t_f)^{\frac{1}{n}-1} = \frac{X^f_{Al_2O_3}}{n \cdot t_f}, \tag{20}$$

  where $X^f_{Al_2O_3}$ denotes the thickness of the remnant Al_2O_3 layer, which is assumed to remain constant, and the values of n and k are the same as those used to describe Al_2O_3 growth. This leads to linear kinetics:

$$X_{Cr_2O_3} = \frac{X^f_{Al_2O_3}}{n \cdot t_f} \cdot (t - t_f)\,. \tag{21}$$

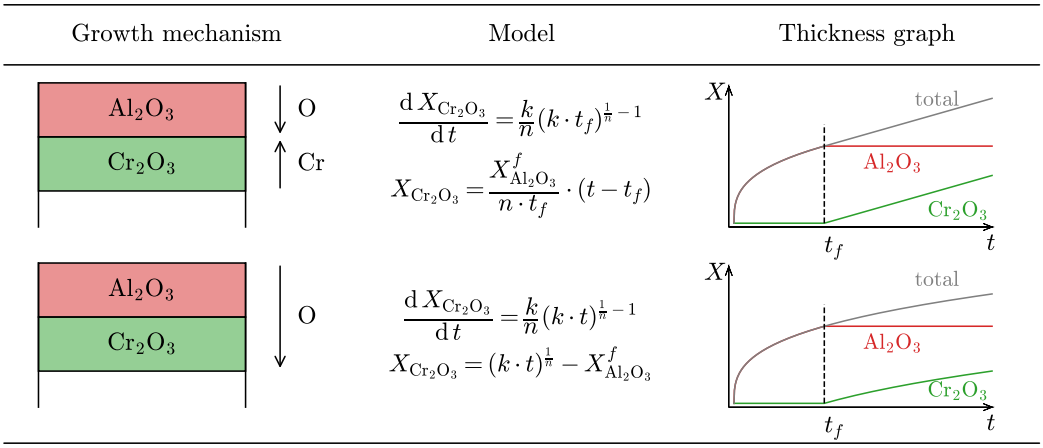

Figure 19: Illustration of the Cr_2O_3 growth mechanisms considered after Al_2O_3 failure, derived from Ref. [16]. See text for symbol definitions.

- Cr_2O_3 grows predominantly by inward O diffusion. The rate-limiting step is O diffusion across both the remnant Al_2O_3 layer and the growing Cr_2O_3. The rate law is not known in general, but in the extreme case where the diffusion properties of Cr_2O_3 are the same as those of Al_2O_3, it simply derives from Eq. (1):

$$\frac{\mathrm{d}X_{Cr_2O_3}}{\mathrm{d}t} = \frac{k}{n}(k \cdot t)^{\frac{1}{n}-1}. \tag{22}$$

  This yields

$$X_{Cr_2O_3} = (k \cdot t)^{\frac{1}{n}} - X^f_{Al_2O_3}, \tag{23}$$

  with, again, the same values of n and k, i.e., cubic kinetics.

The two alternatives are summarized in Fig. 19. We note that neither is quite realistic. Instead, they may be considered as upper and lower bounds: in the "linear kinetics" scenario, Cr_2O_3 growth never slows down, whereas in the "cubic kinetics" scenario, Cr_2O_3 growth slows down as rapidly as Al_2O_3 growth would. The actual kinetics presumably lie in between. Some of the investigators who studied Al_2O_3 failure on FeCrAl alloys described the mass gain curves they obtained in the stage of Cr_2O_3 growth as linear [13, 18]. Depending on the numerical values of the parameters involved (Al_2O_3 growth constants k and n, time to Al_2O_3 failure t_f, total experiment time), the mass gain curves produced by the two scenarios can be quite similar, so much so that they would be impossible to distinguish in practice. This was demonstrated by Strehl et al. [16], who concluded that their data were not sufficient to identify the prevailing growth mechanism.

Two-step simulations (Al_2O_3 growth until failure, then Cr_2O_3 growth according to linear or cubic kinetics) were run with DICTRA for four specimens where experimental profiles had been recorded in the Cr_2O_3 growth stage: UT4B, UT11C, UT4C and UT13B. The profiles obtained for UT4C and UT13B are included in Fig. 13. In UT4C, both linear and cubic scenarios underestimated the Cr consumption, compared to the measured values. In UT13B, on the contrary, both scenarios overestimated Cr consumption — the linear scenario even led to full Cr exhaustion before the end of the 200 h simulation. In UT4C and UT13B, the duration of Cr_2O_3

growth (time elapsed between Al_2O_3 failure and 200 h) was shorter, such that linear and cubic scenarios gave results close to each other, but again both either under- or over-estimated Cr consumption, compared to the experimental results.

The Cr concentration at the end of the 200 h experiment depends on the Cr_2O_3 growth mechanism, but is also quite sensitive to the Al_2O_3 failure time, since the latter determines the time span during which Cr_2O_3 has grown and the state of the specimen (remaining alloy thickness and composition) when Cr_2O_3 started growing. The uncertainty on x_{Cr} is then determined by two antagonistic effects:

- on the one hand, the uncertainty on t_f decreases when h_0 decreases, by virtue of Eq. (11) (in other words, a given spread Δh_0 will result in a larger Δt_f in a thicker specimen);
- on the other hand, the uncertainty on x_{Cr} for a given t_f increases when h_0 decreases (by analogy with Eq. (5), applied to Cr depletion).

In the present case, it appears that the latter effect prevailed. Indeed, neither scenario offered a consistent match to the experimental results. The absence of a consistent trend across all specimens indicates that the x_{Cr} values were strongly affected by experimental variability. As a consequence, it was not possible to determine which mechanism best described Cr_2O_3 growth on the basis of profiles recorded at a few locations.

5 Conclusions

This work analyzed thermodynamic, mechanistic and kinetic aspects of the oxidation of thin NiCoCrAlY foils at 1150 °C, before and after the intrinsic chemical failure of the initially formed Al_2O_3 scale. The comparison of simulated and measured composition profiles showed that the simulations correctly reproduced the alloy response to oxidation, within experimental error. Compositions in the thinner specimens showed some variability; the latter was similar in amplitude to the variations expected from the experimental uncertainty on the initial alloy thickness.

The time evolution of the alloy composition during the stage of Al_2O_3 growth was described with an analytical expression, based on the approximation of flat profiles. This was used to compute quantities of interest in the assessment of thin component lifetime: the time required to fully dissolve the β phase and the time to Al_2O_3 failure. The error made in neglecting the metal recession was evaluated.

Insofar as the flat profile approximation is valid, the time evolution of the alloy composition is insensitive to the alloy diffusion properties, and therefore, the simulation results do not significantly depend on the input diffusion data. The thermodynamics data, however, remain an important factor in computing quantities relying on phase equilibria: phase compositions and fractions, or the time for β dissolution for instance. In this respect, the CRALDAD database appeared to be better suited than TCNI8 to simulate the response of NiCoCrAlY alloys to oxidation, because of a more accurate description of the γ–β equilibrium.

Experimentally, the time-to-Al_2O_3 failure was subject to important local variations within the specimens. These were greater than the variations expected from the uncertainty on the initial alloy thickness. It is concluded that other sources of variability, such as casting defects, were in effect; their impact on Al consumption should be quantified in order to estimate the uncertainty associated with a predicted time-to-failure.

After it failed, the alumina remained present as a continuous layer. The Cr_2O_3 that formed underneath was found to grow much slowlier than it would in the absence of the remnant Al_2O_3 layer. Following the same sequence as that observed for Al_2O_3, Cr_2O_3 growth consumed Cr, the alloy Cr content gradually decreased until the Cr activity was too low to maintain Cr_2O_3 stability, and Ni- and Co-containing spinel oxides formed instead. As Ni and Co oxidized and diffused across the remnant Al_2O_3, spinel layers developed both at the Al_2O_3-gas interface and at the alloy-Cr_2O_3 interface, eventually converting both corundum layers to spinel. Finally, as the oxygen pressure further increased at the alloy surface, the remaining NiCo alloy was converted to (Ni,Co)O, which caused the rupture of the scale and the formation of (Ni,Co)O nodules above it. The small amount of metal left to oxidize at this stage explains the absence of a sharp increase of the mass gain, i.e., the absence of breakaway.

Acknowledgements

The authors thank Brian Gleeson (University of Pittsburgh) for providing the cast alloys. This work was supported in part by the Agence Nationale de la Recherche (France), grant numbers ANR-18-CE08-0003 and ANR-19-CE08-0004.

Conflict of interest

The authors declare that they have no conflict of interest.

References

[1] D. Young. *High temperature oxidation and corrosion of metals*. 2nd. Elsevier, 2016. ISBN: 978-0-08-100101-1. DOI: 10.1016/C2014-0-00259-6.

[2] C. Wagner. "Reaktionstypen bei der Oxydation von Legierungen". *Zeitschrift fur Elektrochemie* 63 (1959), pp. 772–790.

[3] R. A. Rapp. "The transition from internal to external oxidation and the formation of interruption bands in silver-indium alloys". *Acta metallurgica* 9 (1961), pp. 730–741. DOI: 10.1016/0001-6160(61)90103-1.

[4] C. Wagner. "Theoretical analysis of the diffusion processes determining the oxidation rate of alloys". *Journal of the electrochemical society* 99 (1952), pp. 369–380.

[5] H. E. Evans, A. T. Donaldson, and T. C. Gilmour. "Mechanisms of breakaway oxidation and application to a chromia-forming steel". *Oxidation of metals* 52 (1999), pp. 379–402.

[6] D. Texier, D. Monceau, Z. Hervier, and E. Andrieu. "Effect of interdiffusion on mechanical and thermal expansion properties at high temperature of a MCrAlY coated Ni-based superalloy". *Surface and coatings technology* 307 (2016), pp. 81–90. DOI: 10.1016/j.surfcoat.2016.08.059.

[7] W. J. Quadakkers and K. Bongartz. "The prediction of breakaway oxidation for alumina forming ODS alloys using oxidation diagrams". *Materials and corrosion* 45 (1994), 232–241. DOI: 10.1002/maco.19940450404.

[8] B. D. Bastow, D. P. Whittle, and G. C. Wood. "Alloy depletion profiles resulting from preferential removal of less noble-metal during alloy oxidation". *Oxidation of metals* 12 (1978), pp. 413–438. DOI: 10.1007/bf00612088.

[9] J. A. Nesbitt. "Numerical modeling of high-temperature corrosion processes". *Oxidation of metals* 44 (1995), pp. 309–338. DOI: 10.1007/BF01046731.

[10] T. Gheno and G. Lindwall. "On the Simulation of Composition Profiles in NiCoCrAl Alloys During Al_2O_3 Scale Growth in Oxidation and Oxidation–Dissolution Regimes". *Oxidation of metals* 91 (2019), pp. 243–257. DOI: 10.1007/s11085-018-9877-y.

[11] R. Duan, A. Jalowicka, K. Unocic, B. A. Pint, P. Huczkowski, A. Chyrkin, D. Grüner, R. Pillai, and W. J. Quadakkers. "Predicting oxidation-limited lifetime of thin-walled components of NiCrW alloy 230". *Oxidation of metals* 87 (2017), pp. 11–38. DOI: 10.1007/s11085-016-9653-9.

[12] R. Newton, M. J. Bennett, J. P. Wilber, J. Nicholls, D. Naumenko, G. Borchardt, A. Kolb-Telipes, B. Jonsson, A. Westerlund, V. Guttman, M. Maier, and P. Beaven. "Lifetime modelling of high temperature corrosion processes". *Efc publication no. 34*. Ed. by M. Schutze, W. Quadakkers, and J. Nicholls. IoM Communications, 2001, 15–36.

[13] K. Ishii, M. Kohno, and S. Ishikawa. "Effect of rare-earth elements on high-temperature oxidation resistance of Fe-20Cr-5Al alloy foils". *Materials transactions, jim* 38 (1997), pp. 787–792.

[14] N. Hiramatsu and F. H. Stott. "The effect of lanthanum on the scales developed on thin foils of Fe-20Cr-5Al at very high temperatures". *Oxidation of metals* 51 (1999), pp. 479–494. DOI: 10.1023/A:1018891211160.

[15] H. Al-Badairy, G. J. Tatlock, and M. J. Bennett. "A comparison of breakaway oxidation in wedge-shaped and parallel sided coupons of FeCrAl alloys". *Materials at high temperatures* 17 (2000), pp. 101–107. DOI: 10.1179/mht.2000.016.

[16] G. Strehl, D. Naumenko, H. Al-Badairy, L. M. Rodriguez Lobo, G. Borchardt, G. J. Tatlock, and W. Quadakkers. "The effect of aluminium depletion on the oxidation behaviour of FeCrAl foils". *Materials at high temperatures* 17 (2000), pp. 87–92. DOI: 10.1179/mht.2000.014.

[17] G. Tatlock, H. Al-Badairy, M. Bennett, and J. Nicholls. "Characterisation studies of chromia formation on commercial FeCrAlRE alloy foils following chemically induced failure at 900°C". *Materials at high temperatures* 22 (2005), pp. 467–472. DOI: 10.1179/mht.2005.056.

[18] G. J. Tatlock, H. Al-Badairy, M. J. Bennett, R. Newton, J. R. Nicholls, and A. Galerie. "Air oxidation of commercial FeCrAlRE alloy foils between 800 and 950°C". *Materials science and technology* 21 (2005), 893–900. DOI: 10.1179/174328405X46123.

[19] D. J. Young, A. Chyrkin, J. He, D. Gruener, and W. J. Quadakkers. "Slow transition from protective to breakaway oxidation of Haynes 214 foil at high temperature". *Oxidation of metals* 79 (2013), pp. 405–427. DOI: 10.1007/s11085-013-9364-4.

[20] A. Chyrkin, N. Mortazavi, M. Halvarsson, D. Gruener, and W. J. Quadakkers. "Effect of thermal cycling on protective properties of alumina scale grown on thin Haynes 214 foil". *Corrosion science* 98 (2015), pp. 688–698. DOI: 10.1016/j.corsci.2015.06.020.

[21] P. Niranatlumpong, C. B. Ponton, and H. E. Evans. "The failure of protective oxides on plasma-sprayed NiCrAlY overlay coatings". *Oxidation of metals* 53 (2000), 241–258. DOI: 10.1023/A:1004549219013.

[22] H. E. Evans and M. P. Taylor. "Diffusion cells and chemical failure of MCrAlY bond coats in thermal-barrier coating systems". *Oxidation of metals* 55 (2001), 17–34. DOI: 10.1023/A:1010369024142.

[23] D. Texier, M. Ecochard, T. Gheno, D. Monceau, M. Salem, and P. Lours. "Screening for Al_2O_3 failure in MCrAlY APS coatings using short-term oxidation at high temperature". *Corrosion science* 184 (2021), p. 109334. DOI: 10.1016/j.corsci.2021.109334.

[24] J. Andersson, T. Helander, L. Höglund, P. Shi, and B. Sundman. "Thermo-Calc & DICTRA, computational tools for materials science". *Calphad: computer coupling of phase diagrams and thermochemistry* 26.2 (2002), pp. 273–312. ISSN: 03645916. DOI: 10.1016/S0364-5916(02)00037-8.

[25] T. Gheno and B. Gleeson. "Modes of deposit-induced accelerated attack of MCrAlY systems at 1100 °C". *Oxidation of metals* 87 (2017), pp. 249–270. DOI: 10.1007/s11085-016-9669-1.

[26] T. Gheno, X. L. Liu, G. Lindwall, Z.-K. Liu, and B. Gleeson. "Experimental study and thermodynamic modeling of the Al-Co-Cr-Ni system". *Science and technology of advanced materials* 16 (2015), p. 055001. DOI: 10.1088/1468-6996/16/5/055001.

[27] X. L. Liu, G. Lindwall, T. Gheno, and Z.-K. Liu. "Thermodynamic modeling of Al–Co–Cr, Al–Co–Ni, Co–Cr–Ni ternary systems towards a description for Al–Co–Cr–Ni". *Calphad* 52 (2016), pp. 125–142. DOI: 10.1016/j.calphad.2015.12.007.

[28] Materials Preparation Center, Ames Laboratory USDOE, Ames, IA (USA).

[29] D. Texier, D. Monceau, J.-C. Salabura, R. Mainguy, and E. Andrieu. "Micromechanical testing of ultrathin layered material specimens at elevated temperature". *Materials at high temperatures* 33.4-5 (2016), pp. 325–337. DOI: 10.1080/09603409.2016.1182250.

[30] N. Saunders and A. P. Miodownik. *Calphad (calculation of phase diagrams): a comprehensive guide*. Elsevier, 1998.

[31] H. Lukas, S. Fries, and B. Sundman. *Computational thermodynamics: the calphad method*. Cambridge University Press, 2007.

[32] *Thermo-Calc Software MOBNI5 Ni-alloys Mobility Database*.

[33] *Thermo-Calc Software TCNI8 Ni-based Superalloys Database*.

[34] D. Naumenko, B. Gleeson, E. Wessel, L. Singheiser, and W. J. Quadakkers. "Correlation between the microstructure, growth mechanism, and growth kinetics of alumina scales on a FeCrAlY alloy". *Metallurgical and materials transactions a* 38 (2007), pp. 2974–2983. DOI: 10.1007/s11661-007-9342-z.

[35] D. J. Young, D. Naumenko, L. Niewolak, E. Wessel, L. Singheiser, and W. J. Quadakkers. "Oxidation kinetics of Y-doped FeCrAl-alloys in low and high p_{O_2} gases". *Materials and corrosion-Werkstoffe und Korrosion* 61 (2010), pp. 838–844. DOI: 10.1002/maco.200905432.

[36] L. Bataillou, C. Desgranges, L. Martinelli, and D. Monceau. "Modelling of the effect of grain boundary diffusion on the oxidation of Ni-Cr alloys at high temperature". *Corrosion science* 136 (2018), 148–160. DOI: 10.1016/j.corsci.2018.03.001.

[37] *Physical constants of inorganic compounds, in* CRC Handbook of Chemistry and Physics*, ed. D.R. Lide, 89th ed. (CRC Press, Boca Raton, 2008), pp. 4–45.*

[38] T. Gheno and B. Gleeson. "On the reaction mechanism of MCrAlY alloys with oxide-sulfate deposits at 1100 °C". *Oxidation of metals* 86 (2016), pp. 385–406. DOI: 10.1007/s11085-016-9649-5.

[39] D. J. Young, A. Chyrkin, and W. J. Quadakkers. "A simple expression for predicting the oxidation limited life of thin components manufactured from fcc high temperature alloys". *Oxidation of metals* 77 (2012), pp. 253–264. DOI: 10.1007/s11085-012-9283-9.

[40] T. J. Nijdam and W. G. Sloof. "Modelling of composition and phase changes in multiphase alloys due to growth of an oxide layer". *Acta materialia* 56 (2008), pp. 4972–4983. DOI: 10.1016/j.actamat.2008.06.010.

[41] M. S. A. Karunaratne, S. L. Ogden, S. D. Kenny, and R. C. Thomson. "A multicomponent diffusion model for prediction of microstructural evolution in coated Ni based superalloy systems". *Materials science and technology* 25 (2009), pp. 287–299. DOI: 10.1179/174328408X355415.

[42] M. Bensch, A. Sato, N. Warnken, E. Affeldt, R. Reed, and U. Glatzel. "Modelling of high temperature oxidation of alumina-forming single-crystal nickel-base superalloys". *Acta materialia* 60 (2012), pp. 5468–5480. DOI: 10.1016/j.actamat.2012.06.036.

[43] K. Yuan, R. Eriksson, R. L. Peng, X.-H. Li, S. Johansson, and Y.-D. Wang. "Modeling of microstructural evolution and lifetime prediction of MCrAlY coatings on nickel based superalloys during high temperature oxidation". *Surface and coatings technology* 232 (2013), pp. 204–215. DOI: 10.1016/j.surfcoat.2013.05.008.

[44] R. Pillai, W. G. Sloof, A. Chyrkin, L. Singheiser, and W. J. Quadakkers. "A new computational approach for modelling the microstructural evolution and residual lifetime assessment of MCrAlY coatings". *Materials at high temperatures* 32 (2015), pp. 57–67. DOI: 10.1179/0960340914Z.00000000063.

[45] R. Pillai, S. S. Raiman, and B. A. Pint. "First steps toward predicting corrosion behavior of structural materials in molten salts". *Journal of nuclear materials* 546 (2021), p. 152755. DOI: 10.1016/j.jnucmat.2020.152755.

[46] J. Philibert. *Atom movements - diffusion and mass transport in solids*. Les Editions de Physique, 1991.

[47] P. Saltykov, O. Fabrichnaya, J. Golczewski, and F. Aldinger. "Thermodynamic modeling of oxidation of Al–Cr–Ni alloys". *Journal of alloys and compounds* 381 (2004), pp. 99–113. DOI: 10.1016/j.jallcom.2004.02.053.

[48] E. Schmucker, C. Petitjean, L. Martinelli, P.-J. Panteix, S. Ben Lagha, and M. Vilasi. "Oxidation of Ni-Cr alloy at intermediate oxygen pressures. I. diffusion mechanisms through the oxide layer". *Corrosion science* 111 (2016), pp. 474–485. DOI: 10.1016/j.corsci.2016.05.025.

[49] P. Kofstad. *High temperature corrosion*. Elsevier, London, 1988.

[50] L. Latu-Romain, Y. Parsa, S. Mathieu, M. Vilasi, M. Ollivier, A. Galerie, and Y. Wouters. "Duplex n- and p-type chromia grown on pure chromium: a photoelectrochemical and microscopic study". *Oxidation of metals* 86 (2016), 497–509. DOI: 10.1007/s11085-016-9648-6.

[51] L. Latu-Romain, S. Mathieu, M. Vilasi, G. Renou, S. Coindeau, A. Galerie, and Y. Wouters. "The role of oxygen partial pressure on the nature of the oxide scale on a NiCr model alloy". *Oxidation of metals* 88 (2017), 481–493. DOI: 10.1007/s11085-016-9670-8.